ACS Photonics

Article

Cite This: ACS Photonics 2019, 6, 2562−2569

pubs.acs.org/journal/apchd5

Current-Driven Terahertz Light Emission from Graphene Plasmonic Oscillations

Yuyu Li, Pablo Ferreyra, Anna K. Swan, and Roberto Paiella*

Department of Electrical and Computer Engineering and Photonics Center, Boston University, 8 Saint Mary's Street, Boston, Massachusetts 02215, United States

Supporting Information

ABSTRACT: Graphene is a promising materials system for basic studies and device applications in THz optoelectronics with several key functionalities, including photodetection and optical modulation, already demonstrated in recent years. The use of plasmonic excitations in this context is particularly attractive by virtue of their dynamic gate tunability across the far-infrared spectrum, relatively long lifetimes, and highly subwavelength confinement. Here these favorable properties are exploited for the generation of narrowband tunable THz radiation from current-driven plasmonic oscillations. We employ arrays of graphene nanoribbons, where localized plasmonic resonances are excited by an injected electrical current (through the generation and subsequent energy relaxation of hot carriers) and then radiate into the far field. Pronounced emission peaks are correspondingly measured at tunable frequencies across a wide portion of the THz spectrum (4−8 THz), controlled by design through the ribbon width and actively through the applied gate voltage. These results provide a new path for the study of plasmonic and hot-carrier phenomena in graphene and are technologically relevant for the development of highly miniaturized and broadly tunable THz radiation sources.

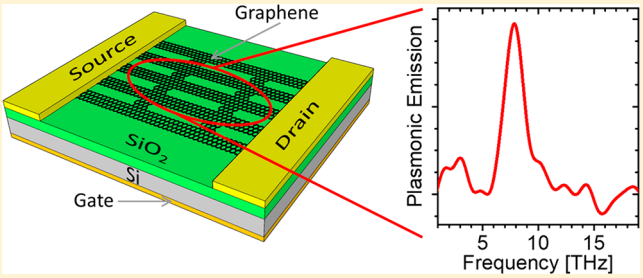

KEYWORDS: *graphene, plasmonics, terahertz optoelectronics, hot-carrier effects, thermal radiation*

Plasmonic excitations in graphene sheets and nanostructures are of significant fundamental and applied interest because of several distinctive and desirable properties compared to traditional systems based on noble metals.[1] In general, collective oscillations of the electron (or hole) gas in graphene can produce guided electromagnetic waves with particularly strong subwavelength field confinement and slow phase velocity. Unlike surface plasmons in noble metals, the dispersion curves and resonance frequencies of these excitations can be tuned actively through the application of a gate voltage (as a means to control the carrier density), which can add significant flexibility and functionality for device applications. For typical graphene carrier densities on the order of several 10^{12} cm^{-2}, plasmonic resonances at mid-infrared and terahertz frequencies are obtained (as opposed to the visible or near-infrared excitations of traditional metal-based systems). As a result, the use of graphene is promising to create new application opportunities for plasmonic science and technology. Finally, the availability of graphene samples with record high carrier mobility at room temperature allows for plasmonic modes with particularly large propagation lengths and spectrally narrow line widths. These considerations have motivated extensive work in recent years, where graphene plasmons have been measured using nanoprobes[2,3] or in transmission measurements with various geometries designed to compensate for their momentum mismatch with free-space radiation (nanoribbons,[4−7] nanoparticles,[8−10] continuous films near a diffraction grating,[11,12] and antidot arrays[10,13,14]). Several device functionalities at both mid-infrared and THz wavelengths have also been proposed and investigated, including photodetectors,[15−18] light emitters,[19−21] optical modulators,[22,23] and biosensors.[24,25]

In the field of THz optoelectronics, a particularly interesting application of plasmonics is the direct conversion of the collective charge oscillations that are intrinsic to any plasma wave into free-space radiation. In its simplest implementation, the underlying radiation mechanism could be described as thermal emission resonantly enhanced by the excitation of surface plasmons, producing significant spectral reshaping. Importantly, this process can be driven electrically through the injection of a current in a two-dimensional electron gas (2DEG) to produce a hot carrier distribution, which can then partially decay into surface plasmons. Therefore, it may form the basis for the development of extremely miniaturized and widely tunable THz optoelectronic oscillators, a class of devices that is still highly underdeveloped.[26] This idea has already been investigated in early work with grating-coupled 2DEGs in traditional semiconductor heterojunctions, such as Si/SiO_2 and GaAs/AlGaAs.[27−29] Pronounced tunable THz emission peaks from thermally excited surface plasmons have been measured in these systems under current injection at

Received: July 17, 2019
Published: September 4, 2019

DOI: 10.1021/acsphotonics.9b01037
ACS Photonics 2019, 6, 2562−2569

cryogenic temperatures and used to study hot-carrier effects and plasmonic dispersion properties. More complex excitation mechanisms have also been proposed[30] involving quasi-ballistic carrier injection across a gated 2DEG to produce a plasma instability, leading to the possibility of high-power coherent emission.

The use of graphene in this general context is once again attractive because of its exceptional transport properties, allowing for ultrahigh carrier mobility and therefore reduced plasmonic damping. As a result, particularly narrow plasmonic emission spectra can be expected even under purely thermal excitation conditions.[31] Graphene is also an ideal materials system for the excitation of hot carriers, by virtue of its very low electronic heat capacity and weak electron−phonon coupling.[32] In this respect it should be noted that prior work has already highlighted the promise of graphene as a stable and efficient thermal emitter at mid-infrared[33] and even visible[34] wavelengths, including a report of plasmon-assisted mid-infrared radiation from an unbiased sample on a heater block.[21] Similarly, the strong confinement of graphene plasmons in the supporting 2DEG is favorable to enhance light−matter interactions, including plasmon generation via hot-carrier decay. In fact, it has been suggested that the latter process can become remarkably efficient and lead to unusual effects (such as the generation of shockwaves) as a result of the unique combination of slow plasmonic phase velocities and high carrier speeds in graphene.[35]

The development of an experimental platform for the investigation of plasmonic THz light emission from graphene would therefore be of interest for fundamental studies of nonequilibrium carrier dynamics and light−matter interaction at the nanoscale, as well as technological advances in optoelectronics. However, despite extensive work on graphene for THz device applications in the past several years,[15,17,19,20,36−51] the measurement of resonant gate-tunable THz light emission from graphene surface plasmons has not been reported yet. To address this goal, here we employ the localized plasmon modes of graphene nanoribbons, involving collective oscillations of the 2DEG in the direction perpendicular to the ribbon axis, at a resonance frequency determined by the ribbon width and graphene charge density.[4−7] Compared to other geometries used to couple free-space radiation to graphene plasmons, nanoribbons are readily compatible with current injection while, at the same time, confining the plasmonic oscillations within localized surface areas, which is favorable to avoid potentially detrimental effects arising from charge-density variations in large-area samples.[12] In our experiments, the nanoribbons are driven with an electrical current, producing a significant increase in the 2DEG temperature over the sample substrate, and sharp emission peaks are correspondingly measured at gate-tunable THz frequencies, in good agreement with theoretical predictions. These spectra could be recorded up to a maximum substrate temperature of about 190 K (partly limited by the lock-in detection scheme used in our measurements), with the electron gas heated up to about room temperature. A simple model of the underlying radiation process is also presented, suggesting that substantial margins of improvement exist with further advances in sample quality and device geometry.

RESULTS AND DISCUSSION

A schematic illustration of the device structures employed in this work and a scanning electron microscopy (SEM) image of an experimental sample are shown in Figure 1a and in the inset

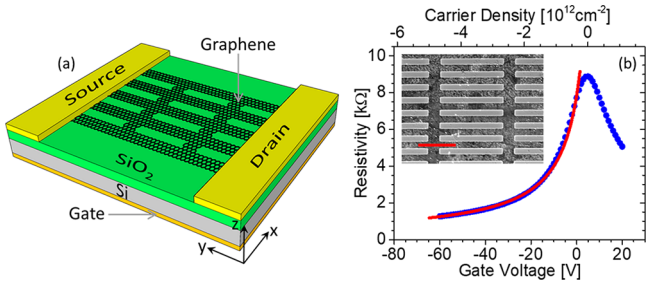

Figure 1. Graphene-nanoribbon THz light emitters. (a) Schematic device structure. (b) Electrical characteristics of an experimental sample (device EMT1). Symbols: resistivity measured as a function of gate voltage V_{GS} at 300 K. The top horizontal axis shows the corresponding carrier density. Solid line: numerical fit to the hole side of the experimental data based on the model discussed in ref 52, from which a hole mobility of 1130 $cm^2/(V\ s)$ is inferred. Inset: top-view SEM image of the same device, showing several neighboring nanoribbons (darker horizontal stripes) connected to one another by perpendicular bridge sections. The scale bar is 3 μm.

of Figure 1b, respectively. In the following, we present data measured with two devices, labeled EMT1 and EMT2, consisting of nanoribbons with 530 and 810 nm widths, respectively, arranged in an array with approximately 50% duty cycle. Both devices are based on large-area films of commercial graphene grown by chemical vapor deposition (CVD) on copper foil, transferred onto oxidized Si substrates with a poly(methyl methacrylate) (PMMA) transfer polymer. A square section of approximately 190 μm side length is defined in the graphene sheets and shaped into the desired nanoribbon pattern by electron-beam lithography and reactive ion etching, followed by fabrication of the metal contacts (see Methods for more details). The nanoribbons run across each device between the source and drain electrodes (horizontally in the inset of Figure 1b) and are connected to one another by small perpendicular "bridge" sections (having 0.9 μm width and 6 μm pitch in sample EMT1, 1.4 μm width and 9 μm pitch in sample EMT2). The purpose of the bridges is to ensure that the presence of even a single crack in a ribbon does not compromise the current flow across the entire ribbon,[6,7] so that the largest possible fraction of the graphene active area can participate in the radiation process. The electrical characteristics (resistivity vs gate voltage V_{GS}) of device EMT1 at 300 K are shown by the symbols in Figure 1b, together with a numerical fit[52] applied to the hole side of the experimental data (solid line). The hole mobility extrapolated from this fit (approximately 1130 $cm^2/(V\ s)$) is on par with typical values measured with CVD graphene deposited on SiO_2 using PMMA,[53] suggesting good overall quality of the patterned nanoribbons.

In this device geometry, each nanoribbon section between consecutive bridges act as a Fabry−Perot cavity for plasma waves along the direction perpendicular to the ribbon axis (the x direction of Figure 1a). The plasmonic resonance frequencies ω_n are then determined by the phase condition requiring constructive interference upon each roundtrip within the cavity,[4−7] that is, $2\mathrm{Re}[\beta(\omega_n)]w + 2\varphi_r = 2n\pi$, where $\beta(\omega)$ is the

DOI: 10.1021/acsphotonics.9b01037
ACS Photonics 2019, 6, 2562−2569

frequency-dependent complex wavenumber of plasmon polaritons in graphene, w is the ribbon width, φ_r is the reflection phase for plasma waves at each ribbon edge, and n is an integer. An analytical expression for the dispersion relation $\beta(\omega)$ can be derived using a simple Drude model for the graphene dynamic conductivity in the nonretarded regime ($\beta \ll \omega/c$).[54] Using this expression, we obtain

$$\omega_n = \sqrt{\frac{q^2 v_F (n\pi - \varphi_r)}{\sqrt{\pi}\hbar\epsilon_0(\epsilon_{r1} + \epsilon_{r2})}}\frac{N^{1/4}}{\sqrt{w}} \quad (1)$$

where $v_F \approx 1 \times 10^8$ cm/s is the Fermi velocity, N is the carrier density, and ϵ_{r1} and ϵ_{r2} are the relative permittivities of the surrounding materials (the Si/SiO_2 substrate and the air above). According to eq 1, the nanoribbon plasmonic resonances can be tuned geometrically by varying the ribbon width w and actively by controlling the carrier density N through the back-gate voltage in the field-effect-transistor geometry of Figure 1a. Specifically, N is determined by the capacitor relation $qN = \epsilon_0\epsilon_{OX}|V_G - V_{CNP}|/t_{OX}$, where ϵ_{OX} and t_{OX} are the permittivity and thickness of the SiO_2 gate dielectric, respectively, V_G is the voltage difference between the back gate and the graphene channel, and V_{CNP} is the gate voltage at charge neutrality. The resulting ability to tune the plasmonic absorption or emission frequency dynamically with an electrical signal is particularly attractive for device applications.

For both samples, EMT1 and EMT2, with carrier densities of several 10^{12} cm^{-2}, eq 1 predicts resonance frequencies in the THz spectral region. In general, the measurement of radiation at these frequencies is complicated by the presence of a strong thermal background from the surrounding environment, which can severely obscure the signal of interest, particularly in the case of small devices such as the samples under study. As a result, we employ a lock-in detection scheme where the current injected into the nanoribbons is modulated at a low frequency (200 Hz) and a lock-in amplifier is used to isolate the detected signal varying at the same frequency from the thermal background. In these measurements, the samples are mounted on the coldfinger of a continuous-flow cryostat, and their emission is detected with a liquid-He-cooled Si bolometer in a Fourier transform infrared (FTIR) spectrometer operated in step-scan mode. The measured traces therefore correspond to the difference between the nanoribbon emission spectra with and without the injected current, without any contribution from the surrounding environment. In passing, we note that the very low modulation frequency used in this work is limited by the bandwidth of the bolometer (400 Hz). In fact, high-speed modulation capabilities can be expected from the same devices, because the underlying radiation process involves ultrafast carrier relaxation dynamics.

Representative results are shown by the red trace in Figure 2a, measured from the device EMT1 gated with a voltage between the gate and source contacts $V_{GS} = V_{CNP} - 75$ V (where $V_{CNP} = -20$ V in this case) at a substrate base temperature T_{base} of 80 K. A pronounced peak near 7.9 THz, attributed to the nanoribbon plasmonic oscillations, is observed over the broader thermal emission from the same active material (the 2DEG greybody radiation reshaped by the spectral transfer function of the measurement setup). In order to more clearly highlight the plasmonic contribution, in Figure 2a, we also plot the emission spectrum measured with the same sample at the same cryostat temperature, but gated at charge

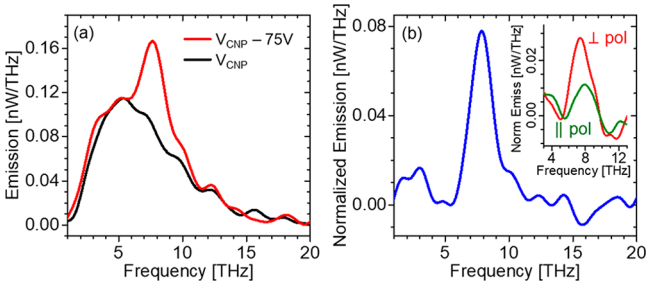

Figure 2. Graphene-nanoribbon THz emission spectra. (a) Measured radiation spectrum of the device EMT1 for $V_{GS} = V_{CNP} - 75$ V (red trace) and $V_{GS} = V_{CNP}$ (black trace). Both traces were obtained at a base temperate T_{base} of 80 K and with an input electrical power P_{in} of 0.2 W. (b) Difference between the two spectra of (a), showing the plasmonic contribution to the measured light. Inset: normalized plasmonic emission peak of the same device under similar conditions, measured through a polarization filter with its transmission axis perpendicular (red trace) and parallel (green trace) to the long axis of the nanoribbons.

neutrality, that is, for $V_{GS} = V_{CNP}$ (black trace). Because the device resistance R increases with decreasing carrier density, in the latter measurement we also increase the voltage V_{DS} between the drain and source contacts (from +21 to +36 V) so as to produce the same electrical power $P_{in} = (V_{DS}^2)/R$ (0.2 W) fed into the device. At charge neutrality, there are not enough carriers present in the graphene channel to allow for any significant thermal excitation (and subsequent radiative decay) of plasmonic oscillations. Correspondingly, the resonance feature near 7.9 THz essentially disappears from the emission spectrum, and only the broader greybody contribution is observed. The difference between these red and black traces, consisting of a sharp peak with a quality factor of about 4 (Figure 2b), therefore, provides a direct measure of the plasmonic contribution to the device output radiation.

All normalized emission spectra presented below are similarly obtained by subtracting off the spectra measured under otherwise identical conditions at charge neutrality. In this normalization procedure, the charge-neutrality spectra are sometimes rescaled by a constant factor (generally between 1 and 1.1) to produce a flatter baseline. This small correction, described in more detail in the Supporting Information, is justified by the expected variations in greybody output power with carrier density, even for constant P_{in}, due to the corresponding changes in both emissivity and temperature increment. Polarization-resolved measurements also indicate that the resulting normalized emission peaks are predominantly polarized along the direction perpendicular to the ribbons (the x direction of Figure 1a), as illustrated in the inset of Figure 2b. This behavior is consistent with plasmonic emission, which, in the present samples, can be described as originating from a line of electric-dipole sources oscillating perpendicular to the ribbon axis. The residual signal measured with the orthogonal polarization (green trace in Figure 2b) is attributed to the detection of light radiated over a finite range of angles from the sample surface normal, where the dipole-emission polarization direction can be rotated with respect to the dipole moment. The excitation of plasmonic modes with wavevector at a finite angle with respect to the x axis may also contribute to this residual signal.

The measured devices also exhibit the geometrical and electrostatic tunability described above. To illustrate, Figure 3a

DOI: 10.1021/acsphotonics.9b01037
ACS Photonics 2019, 6, 2562−2569

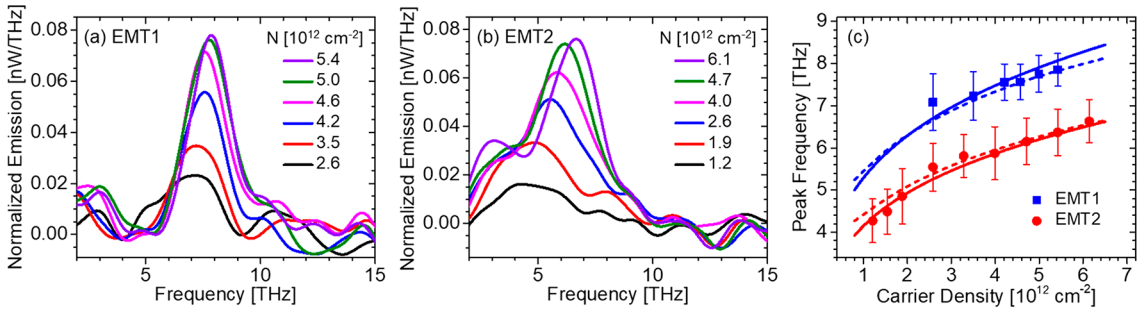

Figure 3. Spectral tunability of plasmonic emission from graphene nanoribbons. (a, b) Normalized emission peaks measured with the devices EMT1 (a) and EMT2 (b) for T_{base} = 80 K, P_{in} = 0.2 W, and different values of V_{GS} (with the corresponding hole-density values listed in the legend). (c) Symbols: peak emission frequencies of the spectra measured with EMT1 (squares) and EMT2 (circles) vs carrier density. The vertical bars indicate the spectral range where the emission signal is above 90% of the peak value. Solid lines: numerical fits to the expression for the fundamental plasmonic resonance frequency of eq 1, with the reflection phase φ_r used as the only fitting parameter. Dashed lines: resonance frequencies computed by FDTD simulations for the nanoribbon widths of both devices (w = 530 and 810 nm).

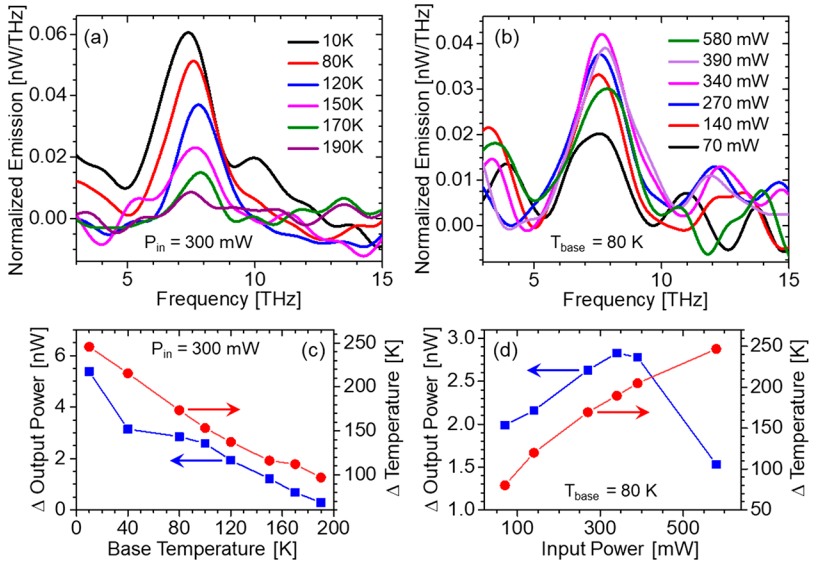

Figure 4. Temperature and input-power dependence of plasmonic emission from graphene nanoribbons. (a) Normalized plasmonic emission peaks measured with the device EMT1 at different base temperatures for P_{in} = 0.3 W. (b) Normalized emission peaks of the same device at T_{base} = 80 K for different values of the input electrical power. (c, d) Plasmonic output power ΔP_{pl} and electronic temperature increment $\Delta T = T_{el} - T_{base}$ (near the source contact) vs base temperature (c) and vs input power (d). In all these measurements, the applied gate voltage is nominally $V_{GS} = V_{CNP} - 60$ V.

and b show a selection of normalized emission spectra measured with EMT1 and EMT2, respectively, at different gate voltages V_{GS} for T_{base} = 80 K and P_{in} = 0.2 W. An obvious blue shift in the frequency of peak emission with increasing carrier density is observed with both devices. Furthermore, for the same carrier density, the narrower-nanoribbon device, EMT1, consistently emits at higher frequencies. These observations are summarized in Figure 3c, where the symbols show the measured emission frequencies as a function of hole density N (computed with the gate capacitor relation from the applied voltage V_{GS}), with the vertical bars indicating the spectral range where the emission signal is above 90% of the peak value. The solid lines are numerical fits to eq 1 for the frequency of the fundamental plasmonic resonance (i.e., for n = 1), with the reflection phase φ_r used as the only fitting parameter for both traces. Finally, the dashed lines indicate the plasmonic resonance frequencies of the same nanoribbons computed with the finite difference time domain (FDTD) method, without any free parameters. Both fitting procedure and numerical simulations (described in more detail in the Supporting Information) produce results in good agreement with the experimental data. This observation confirms the plasmonic origin of the measured emission peaks and highlights the validity of the simple model of eq 1. Furthermore, it suggests that the value of φ_r extrapolated from the numerical fit (0.6π) is also approximately valid for nanoribbons with ideal straight edges (as modeled in our FDTD simulations), despite the expected presence of structural imperfections and possibly chemical contamination in the experimental samples.

A more quantitative description of the observed radiation mechanism, including an estimate of the output power, requires knowledge of the 2DEG temperature increment ΔT produced by the injected current. This quantity can be evaluated using the heat-transfer model of refs 55−57, where "supercollisions" involving disorder-assisted acoustic-phonon scattering are identified as the dominant cooling mechanism for hot carriers in graphene at temperatures above a characteristic cryogenic value (the Bloch-Grüneisen limit[57]).

DOI: 10.1021/acsphotonics.9b01037
ACS Photonics 2019, 6, 2562−2569

In this regime, which generally applies to our samples, a steady-state solution of the heat-transfer rate equation gives

$$p_{in} = A[T_{el}^3 - T_{latt}^3] \quad (2)$$

where p_{in} is the input electrical power density per unit area, T_{el} and T_{latt} are the electronic and lattice temperatures, respectively, and A is the supercollision coupling constant (proportional to the carrier density N and inversely proportional to the disorder-limited mean free path[55]). Importantly, all variables in eq 2 must be computed as a function of position y along the nanoribbons because of the spatial variations in electrostatic potential produced by the large source-drain voltages, V_{DS}, used in our measurements (up to about 50 V). The lattice temperature generally remains quite close to the base temperature T_{base} (controlled by the cryostat) due to efficient heat dissipation in the Si substrate, and it can be calculated from the relevant thermal resistance. More details about this whole analysis are presented in the Supporting Information.

Given the 2DEG temperature under bias $T_{el}(y)$, the greybody contribution to the output power can then be evaluated using Planck's law, modified to include the experimental value of 1.6% for the emissivity of unpatterned graphene[33] and integrated over the entire length of the nanoribbons. As discussed above, the nanoribbon output spectra measured at charge neutrality predominantly consist of this greybody contribution. When the device is gated away from charge neutrality, a large increase in detected signal is observed at the plasmonic resonance frequency. Given knowledge of the greybody radiation output, this observed increase can then be used to estimate the optical power ΔP_{pl} of the plasmonic peak. For example, in Figure 2a, the detected signal at the plasmonic resonance frequency increases by a factor of 1.9 in going from charge neutrality (black trace) to $V_{GS} = V_{CNP} - 75$ V (red trace). The value of ΔP_{pl} correspondingly obtained from this analysis is 3.4 nW (see Supporting Information), equivalent to an output power density per unit device-active-area of about 20 μW/cm^2. In passing we note that the fraction of plasmonic emission power detected by the bolometer under the same conditions $\Delta P_{pl}^{det} = \eta \Delta P_{pl}$ can be estimated by integrating the spectrum of Figure 2b across the entire peak line width, which gives a value of about 0.2 nW. These two power estimates are consistent with one another if we assume a collection and transmission efficiency of our measurement setup η (from the sample to the bolometer) of about 6%, which is quite reasonable.

The analysis just described can be used to evaluate how the plasmonic emission process depends on the substrate base temperature T_{base} and total input electrical power $P_{in} = V_{DS}^2/R$. Figure 4 shows several normalized emission spectra of the device EMT1, measured at different temperatures for $P_{in} = 0.3$ W in panel (a), and for different input powers at $T_{base} = 80$ K in panel (b). The corresponding increments in 2DEG temperature over the substrate $\Delta T = T_{el} - T_{base}$ (at the source side of the nanoribbons) and in plasmonic output power ΔP_{pl} are plotted versus T_{base} in Figure 4c and versus P_{in} in Figure 4d. Similar results are obtained with the device EMT2 (see Supporting Information). A monotonic decrease in ΔP_{pl} with increasing base temperature is observed in Figure 4a,c, and the plasmonic emission peak is no longer resolvable above a maximum T_{base} of about 190 K (with the 2DEG correspondingly heated up to about room temperature). This behavior is partly related to the lock-in detection scheme used in our experiments, where only the increase in output power (ΔP_{pl}) produced by the current-driven temperature increment (ΔT) is measured. As shown in Figure 4c, ΔT decreases with increasing T_{base}, which automatically causes a decrease in ΔP_{pl} (even if the plasmonic emission efficiency remains constant). At the same time, Figure 4b,d shows that ΔP_{pl} initially increases and eventually decreases with increasing P_{in}, with the latter trend suggesting that the radiation efficiency is actually also degraded at sufficiently high temperatures. This behavior can be attributed to an increase in the nonradiative damping rate of the plasmonic oscillations and/or a decrease in the plasmonic excitation rate by the injected hot carriers, due to phonon-related interactions. It should also be noted that the charge-neutrality voltage V_{CNP} was found to become somewhat unstable with increasing T_{base}, as indicated by the variations in peak emission frequency observed in Figure 4a, which further complicates the high-temperature measurements.

Finally, in order to further understand the current limitations and prospects for improvement of the devices under study, we present a simple model adapted from coupled mode theory[58] to describe their radiation efficiency. In this model, the time evolution of the energy $|a|^2$ stored in the fundamental plasmonic resonance of the nanoribbons is governed by the rate equation

$$\dot{a} = -(i\omega_1 + \Gamma_{rad}/2 + \Gamma_{abs}/2)a + \sqrt{\Gamma_{exc} P_{in}} \quad (3)$$

where ω_1 is the resonance frequency of eq 1, Γ_{rad} and Γ_{abs} are, respectively, the radiative and nonradiative (ohmic-absorption) damping rates of the plasmonic oscillations, and Γ_{exc} is the rate at which these oscillations are excited by the input electrical power P_{in}. In this framework, the plasmonic radiation output power is simply $P_{pl} = \Gamma_{rad}|a|^2$, which can be computed as a function of frequency ω from the steady-state solution of eq 3 as follows

$$\frac{P_{pl}}{P_{in}} = \frac{\Gamma_{rad}\Gamma_{exc}}{(\omega - \omega_1)^2 + (\Gamma_{rad} + \Gamma_{abs})^2/4} \quad (4)$$

Importantly, the plasmonic oscillations in our devices are excited through the current-driven generation and subsequent energy relaxation of hot carriers, which occurs through the same scattering mechanisms that are also responsible for the plasmonic nonradiative decay (involving impurities, defects, phonons, geometrical boundaries, and other carriers). Therefore, the excitation rate Γ_{exc} can be expected to increase with increasing absorption rate Γ_{abs}, and vice versa. If this relationship can be assumed to be linear, the peak output power at resonance ($\omega = \omega_1$) becomes proportional to $\Gamma_{rad}\Gamma_{abs}/(\Gamma_{rad} + \Gamma_{abs})^2$, which is maximum for $\Gamma_{rad} = \Gamma_{abs}$. This result (analogous to the critical-coupling condition for optically excited cavity resonances) provides a key design guideline for the further development of these plasmonic THz emitters.

In our present samples, the absorption rate Γ_{abs} can be expected to be significantly larger than the radiative term Γ_{rad}, due to the moderate mobility of CVD graphene on SiO_2, as well as the long radiative lifetime of graphene plasmons in general (related to their particularly large wavevector mismatch with free-space radiation). In fact, prior transmission spectroscopy measurements with similar graphene nanoribbons[4−7] show peak plasmonic absorption values on the order of only a few %, indicating that the ratio $\Gamma_{rad}/\Gamma_{abs}$ is similarly small. As a result, the plasmonic-emission power spectral density of the

DOI: 10.1021/acsphotonics.9b01037
ACS Photonics 2019, 6, 2562−2569

present samples is limited to values of the same order of magnitude as the graphene thermal background (e.g., see Figure 2a). The ratio $\Gamma_{rad}/\Gamma_{abs}$ and, therefore, the output power of eq 4 can be increased by engineering the nanoribbon photonic environment to enhance Γ_{rad}, for example, using cavity effects or additional metallic nanoantennas, along the same lines that are currently being pursued for the demonstration of perfect absorption in graphene.[59,22] Alternatively, ultrahigh-mobility samples could be employed to decrease the nonradiative damping rate Γ_{abs}. In fact, room-temperature plasmonic resonances with particularly narrow line widths and large propagation lengths have already been measured in graphene sheets embedded within highly inert hexagonal BN layers[60] or quasi-freestanding.[61] These structures are therefore particularly promising for the development of plasmonic THz light emitters operating at room base temperature. The radiation efficiency of eq 4 could also be improved by increasing the ratio $\Gamma_{exc}/\Gamma_{abs}$, for example, with more complex graphene channel geometries designed to optimize the temperature spatial profile under bias. Additionally, we note that ultrahigh-mobility graphene samples also allow for ballistic transport across the entire device,[62] except for the contribution of carrier−carrier scattering at high carrier density. This transport regime is the key requirement for the Dyakonov-Shur plasma instability,[30] where resonant plasma waves are amplified as they propagate along the 2DEG. In the presence of a suitable antenna geometry (such as the nanoribbons under study), coherent high-power THz emission could therefore be obtained.

CONCLUSIONS

In summary, we have demonstrated current-driven THz radiation from plasmonic resonances in graphene nanoribbons. These nanostructures provide an ideal materials platform to investigate the complex interaction between plasmons and hot carriers in the low-energy (THz) regime, including the impact of high-mobility and possibly ballistic transport conditions. In passing, it should be noted that the reverse process, where hot carriers are created through the energy relaxation of optically excited plasmonic resonances, is also of significant fundamental interest, with important potential applications including photovoltaics and photocatalysis.[63] With further advances in sample quality and device geometry, the graphene structures presented in this work are also technologically relevant with respect to a key outstanding challenge in solid-state optoelectronics, the development of practical sources of THz radiation. Distinctive features in this respect include very small dimensions, compatibility with a wide range of substrates (including Si-based microelectronics), broadband active tunability of the emission frequency, and the possibility of high-speed modulation.

METHODS

Device Fabrication. The experimental samples are based on commercial graphene grown by CVD on copper foil. Large-area films of this graphene material are transferred onto low-*p*-doped oxidized Si substrates using a layer of PMMA, which is then removed with an acetone bath, followed by a dry anneal process. Prior to the transfer step, the back surface of the Si substrate is coated with the gate contact, consisting of a bilayer of 5 nm Cr and 60 nm Au. Optical and SEM microscopy are used to identify a sufficiently large section of the transferred graphene film having minimal defect density, which is then shaped into the desired nanoribbon pattern by electron-beam lithography and reactive ion etching. Next, the source and drain contacts are fabricated using electron-beam lithography, electron-beam deposition of the electrode materials (again comprising 5 nm of Cr and 60 nm of Au), and liftoff. The completed devices are then soldered on a sapphire substrate on a copper block, with the source, drain, and gate contacts wire-bonded to Au-coated ceramic plates and, finally, mounted on the coldfinger of a continuous-flow liquid-He cryostat.

Radiation Measurements. The devices under study are doped electrostatically with a constant gate voltage V_{GS} and biased with a square-wave voltage signal V_{DS} at a frequency of 200 Hz between the source and drain contacts, with the injected current I_{DS} monitored using a home-built current probe. The radiation output is transmitted through a vacuum-sealed FTIR spectrometer operated in step-scan mode, and finally detected with a liquid-He-cooled Si bolometer and a lock-in amplifier synchronized with the bias voltage. The spectral resolution used in the measurements is typically 32 cm^{-1} (0.96 THz). The power spectral density of the detected light is computed from the voltage measured by the lock-in amplifier, given the nominal responsivity (5500 V/W) and preamplifier gain (200 V/V) of the bolometer.

ASSOCIATED CONTENT

Supporting Information

The Supporting Information is available free of charge on the ACS Publications website at DOI: 10.1021/acsphotonics.9b01037.

Normalization procedure for the plasmonic emission spectra. Data fitting procedure for the plasmonic emission frequency. FDTD simulation results. Electronic temperature analysis. Plasmonic-emission power analysis. Additional measurement results (PDF)

AUTHOR INFORMATION

Corresponding Author

*E-mail: rpaiella@bu.edu.

ORCID

Yuyu Li: 0000-0001-5351-5831

Roberto Paiella: 0000-0002-7183-6249

Notes

The authors declare no competing financial interest.

ACKNOWLEDGMENTS

This work was partly supported by the National Science Foundation under Grant #DMR-1308659. The FDTD simulations were performed using the Shared Computing Cluster facility at Boston University.

REFERENCES

(1) Grigorenko, A. N.; Polini, M.; Novoselov, K. S. Graphene Plasmonics. *Nat. Photonics* **2012**, *6*, 749−758.

(2) Chen, J.; Badioli, M.; Alonso-González, P.; Thongrattanasiri, S.; Huth, F.; Osmond, J.; Spasenović, M.; Centeno, A.; Pesquera, A.; Godignon, P.; Elorza, A. Z.; Camara, N.; García de Abajo, F. J.; Hillenbrand, R.; Koppens, F. H. L. Optical Nano-Imaging of Gate-Tunable Graphene Plasmons. *Nature* **2012**, *487*, 77−81.

(3) Fei, Z.; Rodin, A. S.; Andreev, G. O.; Bao, W.; McLeod, A. S.; Wagner, M.; Zhang, L. M.; Zhao, Z.; Thiemens, M.; Dominguez, G.; Fogler, M. M.; Neto, A. H. C.; Lau, C. N.; Keilmann, F.; Basov, D. N.

DOI: 10.1021/acsphotonics.9b01037
ACS Photonics 2019, 6, 2562−2569

Gate-Tuning of Graphene Plasmons Revealed by Infrared Nano-Imaging. *Nature* **2012**, *487*, 82−85.
(4) Ju, L.; Geng, B.; Horng, J.; Girit, C.; Martin, M.; Hao, Z.; Bechtel, H. A.; Liang, X.; Zettl, A.; Shen, Y. R.; Wang, F. Graphene Plasmonics for Tunable Terahertz Metamaterials. *Nat. Nanotechnol.* **2011**, *6*, 630−634.
(5) Yan, H.; Low, T.; Zhu, W.; Wu, Y.; Freitag, M.; Li, X.; Guinea, F.; Avouris, P.; Xia, F. Damping Pathways of Mid-Infrared Plasmons in Graphene Nanostructures. *Nat. Photonics* **2013**, *7*, 394−399.
(6) Brar, V. W.; Jang, M. S.; Sherrott, M.; Lopez, J. J.; Atwater, H. A. Highly confined tunable mid-infrared plasmonics in graphene nanoresonators. *Nano Lett.* **2013**, *13*, 2541−2547.
(7) Luxmoore, I. J.; Gan, C. H.; Liu, P. Q.; Valmorra, F.; Li, P.; Faist, J.; Nash, G. R. Strong Coupling in the Far-Infrared between Graphene Plasmons and the Surface Optical Phonons of Silicon Dioxide. *ACS Photonics* **2014**, *1*, 1151−1155.
(8) Yan, H.; Li, X.; Chandra, B.; Tulevski, G.; Wu, Y.; Freitag, M.; Zhu, W.; Avouris, P.; Xia, F. Tunable Infrared Plasmonic Devices Using Graphene/Insulator Stacks. *Nat. Nanotechnol.* **2012**, *7*, 330−334.
(9) Fang, Z.; Thongrattanasiri, S.; Schlather, A.; Liu, Z.; Ma, L.; Wang, Y.; Ajayan, P. M.; Nordlander, P.; Halas, N. J.; García de Abajo, F. J. Gated Tunability and Hybridization of Localized Plasmons in Nanostructured Graphene. *ACS Nano* **2013**, *7*, 2388−2395.
(10) Zhu, X.; Wang, W.; Yan, W.; Larsen, M. B.; Bøggild, P.; Pedersen, T. G.; Xiao, S.; Zi, J.; Mortensen, N. A. Plasmon–Phonon Coupling in Large-Area Graphene Dot and Antidot Arrays Fabricated by Nanosphere Lithography. *Nano Lett.* **2014**, *14*, 2907−2913.
(11) Gao, W.; Shi, G.; Jin, Z.; Shu, J.; Zhang, Q.; Vajtai, R.; Ajayan, P. M.; Kono, J.; Xu, Q. Excitation and Active Control of Propagating Surface Plasmon Polaritons in Graphene. *Nano Lett.* **2013**, *13*, 3698−3702.
(12) Tantiwanichapan, K.; Wang, X.; Durmaz, H.; Li, Y.; Swan, A. K.; Paiella, R. Graphene Terahertz Plasmons: a Combined Transmission Spectroscopy and Raman Microscopy Study. *ACS Photonics* **2017**, *4*, 2011−2017.
(13) Yeung, K. Y. M.; Chee, J.; Yoon, H.; Song, Y.; Kong, J.; Ham, D. Far-Infrared Graphene Plasmonic Crystals for Plasmonic Band Engineering. *Nano Lett.* **2014**, *14*, 2479−2484.
(14) Liu, P. Q.; Valmorra, F.; Maissen, C.; Faist, J. Electrically Tunable Graphene Anti-Dot Array Terahertz Plasmonic Crystals Exhibiting Multi-Band Resonances. *Optica* **2015**, *2*, 135−140.
(15) Vicarelli, L.; Vitiello, M. S.; Coquillat, D.; Lombardo, A.; Ferrari, A. C.; Knap, W.; Polini, M.; Pellegrini, V.; Tredicucci, A. Graphene Field-Effect Transistors as Room-Temperature Terahertz Detectors. *Nat. Mater.* **2012**, *11*, 865−871.
(16) Freitag, M.; Low, T.; Zhu, W.; Yan, H.; Xia, F.; Avouris, P. Photocurrent in Graphene Harnessed by Tunable Intrinsic Plasmons. *Nat. Commun.* **2013**, *4*, 1951.
(17) Cai, X.; Sushkov, A. B.; Jadidi, M. M.; Nyakiti, L. O.; Myers-Ward, R. L.; Gaskill, D. K.; Murphy, T. E.; Fuhrer, M. S.; Drew, H. D. Plasmon-Enhanced Terahertz Photodetection in Graphene. *Nano Lett.* **2015**, *15*, 4295−4302.
(18) Guo, Q.; Yu, R.; Li, C.; Yuan, S.; Deng, B.; García de Abajo, F. J.; Xia, F. Efficient Electrical Detection of Mid-Infrared Graphene Plasmons at Room Temperature. *Nat. Mater.* **2018**, *17*, 986−992.
(19) Rana, F. Graphene Terahertz Plasmon Oscillators. *IEEE Trans. Nanotechnol.* **2008**, *7*, 91−99.
(20) Otsuji, T.; Popov, V.; Ryzhii, V. Active Graphene Plasmonics for Terahertz Device Applications. *J. Phys. D: Appl. Phys.* **2014**, *47*, 94006.
(21) Brar, V. W.; Sherrott, M. C.; Jang, M. S.; Kim, S.; Kim, L.; Choi, M.; Sweatlock, L. A.; Atwater, H. A. Electronic Modulation of Infrared Radiation in Graphene Plasmonic Resonators. *Nat. Commun.* **2015**, *6*, 7032.
(22) Kim, S.; Jang, M. S.; Brar, V. W.; Mauser, K. W.; Kim, L.; Atwater, H. A. Electronically Tunable Perfect Absorption in Graphene. *Nano Lett.* **2018**, *18*, 971−979.
(23) Jadidi, M. M.; Daniels, K. M.; Myers-Ward, R. L.; Gaskill, D. K.; König-Otto, J. C.; Winnerl, S.; Sushkov, A. B.; Drew, H. D.; Murphy, T. E.; Mittendorff, M. Optical Control of Plasmonic Hot Carriers in Graphene. *ACS Photonics* **2019**, *6*, 302−307.
(24) Li, Y.; Yan, H.; Farmer, D. B.; Meng, X.; Zhu, W.; Osgood, R. M.; Heinz, T. F.; Avouris, P. Graphene Plasmon Enhanced Vibrational Sensing of Surface-Adsorbed Layers. *Nano Lett.* **2014**, *14*, 1573−1577.
(25) Rodrigo, D.; Limaj, O.; Janner, D.; Etezadi, D.; García de Abajo, F. J. G.; Pruneri, V.; Altug, H. Mid-Infrared Plasmonic Biosensing with Graphene. *Science* **2015**, *349*, 165−168.
(26) Mittleman, D. M. Frontiers in terahertz sources and plasmonics. *Nat. Photonics* **2013**, *7*, 666−669.
(27) Höpfel, R. A.; Vass, E.; Gornik, E. Thermal Excitation of Two-Dimensional Plasma Oscillations. *Phys. Rev. Lett.* **1982**, *49*, 1667−1671.
(28) Okisu, N.; Sambe, Y.; Kobayashi, T. Far-Infrared Emission from Two-Dimensional Plasmons in AlGaAs/GaAs Heterointerfaces. *Appl. Phys. Lett.* **1986**, *48*, 776−778.
(29) Hirakawa, K.; Yamanaka, K.; Grayson, M.; Tsui, D. C. Far-Infrared Emission Spectroscopy of Hot Two-Dimensional Plasmons in $Al_{0.3}Ga_{0.7}As$/GaAs Heterojunctions. *Appl. Phys. Lett.* **1995**, *67*, 2326−2328.
(30) Dyakonov, M.; Shur, M. Shallow Water Analogy for a Ballistic Field Effect Transistor: New Mechanism of Plasma Wave Generation by dc Current. *Phys. Rev. Lett.* **1993**, *71*, 2465−2468.
(31) Manjavacas, A.; Thongrattanasiri, S.; Greffet, J.-J.; García de Abajo, F. J. Graphene Optical-to-Thermal Converter. *Appl. Phys. Lett.* **2014**, *105*, 211102.
(32) Fong, K. C.; Schwab, K. C. Ultrasensitive and Wide-Bandwidth Thermal Measurements of Graphene at Low Temperatures. *Phys. Rev. X* **2012**, *2*, 031006.
(33) Freitag, M.; Chiu, H.-Y.; Steiner, M.; Perebeinos, V.; Avouris, P. Thermal Infrared Emission from Biased Graphene. *Nat. Nanotechnol.* **2010**, *5*, 497−501.
(34) Kim, Y. D.; Kim, H.; Cho, Y.; Ryoo, J. H.; Park, C.-H.; Kim, P.; Kim, Y. S.; Lee, S.; Li, Y.; Park, S.-N.; Yoo, Y. S.; Yoon, D.; Dorgan, V. E.; Pop, E.; Heinz, T. F.; Hone, J.; Chun, S.-H.; Cheong, H.; Lee, S. W.; Bae, M.-H.; Park, Y. D. Bright Visible Light Emission from Graphene. *Nat. Nanotechnol.* **2015**, *10*, 676−681.
(35) Kaminer, I.; Katan, Y. T.; Buljan, H.; Shen, Y.; Ilic, O.; Lopez, J. J.; Wong, L. J.; Joannopoulos, J. D.; Soljačic, M. Efficient Plasmonic Emission by the Quantum Čerenkov Effect from Hot Carriers in Graphene. *Nat. Commun.* **2016**, *7*, 11880.
(36) Boubanga-Tombet, S.; Chan, S.; Watanabe, T.; Satou, A.; Ryzhii, V.; Otsuji, T. Ultrafast Carrier Dynamics and Terahertz Emission in Optically Pumped Graphene at Room Temperature. *Phys. Rev. B: Condens. Matter Mater. Phys.* **2012**, *85*, 035443.
(37) Prechtel, L.; Song, L.; Schuh, D.; Ajayan, P.; Wegscheider, W.; Holleitner, A. W. Time-Resolved Ultrafast Photocurrents and Terahertz Generation in Freely Suspended Graphene. *Nat. Commun.* **2012**, *3*, 646.
(38) Sensale-Rodriguez, B.; Yan, R.; Kelly, M. M.; Fang, T.; Tahy, K.; Hwang, W. S.; Jena, D.; Liu, L.; Xing, H. G. Broadband Graphene Terahertz Modulators Enabled by Intraband Transitions. *Nat. Commun.* **2012**, *3*, 780.
(39) Ren, L.; Zhang, Q.; Yao, J.; Sun, Z.; Kaneko, R.; Yan, Z.; Nanot, S.; Jin, Z.; Kawayama, I.; Tonouchi, M.; Tour, J. M.; Kono, J. Terahertz and Infrared Spectroscopy of Gated Large-Area Graphene. *Nano Lett.* **2012**, *12*, 3711−3715.
(40) Weis, P.; Garcia-Pomar, J. L.; Höh, M.; Reinhard, B.; Brodyanski, A.; Rahm, M. Spectrally Wide-Band Terahertz Wave Modulator Based on Optically Tuned Graphene. *ACS Nano* **2012**, *6*, 9118−9124.
(41) Mittendorff, M.; Winnerl, S.; Kamann, J.; Eroms, J.; Weiss, D.; Schneider, H.; Helm, M. Ultrafast graphene-based broadband THz detector. *Appl. Phys. Lett.* **2013**, *103*, 021113.

DOI: 10.1021/acsphotonics.9b01037
ACS Photonics 2019, 6, 2562−2569

(42) Mikhailov, S. A. Graphene-Based Voltage-Tunable Coherent Terahertz Emitter. *Phys. Rev. B: Condens. Matter Mater. Phys.* **2013**, *87*, 115405.
(43) Tantiwanichapan, K.; Wang, X.; Swan, A. K.; Paiella, R. Graphene on Nanoscale Gratings for the Generation of Terahertz Smith-Purcell Radiation. *Appl. Phys. Lett.* **2014**, *105*, 241102.
(44) Yao, X.; Tokman, M.; Belyanin, A. Efficient Nonlinear Generation of THz Plasmons in Graphene and Topological Insulators. *Phys. Rev. Lett.* **2014**, *112*, 055501.
(45) Bahk, Y.-M.; Ramakrishnan, G.; Choi, J.; Song, H.; Choi, G.; Kim, Y. H.; Ahn, K. J.; Kim, D.-S.; Planken, P. C. M. Plasmon Enhanced Terahertz Emission from Single Layer Graphene. *ACS Nano* **2014**, *8*, 9089−9096.
(46) Cai, X.; Sushkov, A. B.; Suess, R. J.; Jadidi, M. M.; Jenkins, G. S.; Nyakiti, L. O.; Myers-Ward, R. L.; Li, S.; Yan, J.; Gaskill, D. K.; Murphy, T. E.; Drew, H. D.; Fuhrer, M. S. Sensitive Room-Temperature Terahertz Detection via the Photothermoelectric Effect in Graphene. *Nat. Nanotechnol.* **2014**, *9*, 814−819.
(47) Tong, J.; Muthee, M.; Chen, S.-Y.; Yngvesson, S. K.; Yan, J. Antenna Enhanced Graphene THz Emitter and Detector. *Nano Lett.* **2015**, *15*, 5295−5301.
(48) Yadav, D.; Boubanga Tombet, S.; Watanabe, T.; Arnold, S.; Ryzhii, V.; Otsuji, T. Terahertz Wave Generation and Detection in Double-Graphene Layered Van der Waals Heterostructures. *2D Mater.* **2016**, *3*, 045009.
(49) Li, Y.; Paiella, R. Interminiband Optical Transitions in Graphene Lateral Superlattices. *ACS Photonics* **2018**, *5*, 3331−3337.
(50) Yao, B.; Liu, Y.; Huang, S.-W.; Choi, C.; Xie, Z.; Flor Flores, J.; Wu, Y.; Yu, M.; Kwong, D.-L.; Huang, Y.; Rao, Y.; Duan, X.; Wong, C. W. Broadband Gate-Tunable Terahertz Plasmons in Graphene Heterostructures. *Nat. Photonics* **2018**, *12*, 22−28.
(51) Hafez, H. A.; Kovalev, S.; Deinert, J.-C.; Mics, Z.; Green, B.; Awari, N.; Chen, M.; Germanskiy, S.; Lehnert, U.; Teichert, J.; Wang, Z.; Tielrooij, K.-J.; Liu, Z.; Chen, Z.; Narita, A.; Müllen, K.; Bonn, M.; Gensch, M.; Turchinovich, D. Extremely Efficient Terahertz High-Harmonic Generation in Graphene by Hot Dirac Fermions. *Nature* **2018**, *561*, 507−511.
(52) Hong, X.; Zou, K.; Zhu, J. Quantum Scattering Time and Its Implications on Scattering Sources in Graphene. *Phys. Rev. B: Condens. Matter Mater. Phys.* **2009**, *80*, 241415.
(53) Kim, S. J.; Choi, T.; Lee, B.; Lee, S.; Choi, K.; Park, J. B.; Yoo, J. M.; Choi, Y. S.; Ryu, J.; Kim, P.; Hone, J.; Hong, B. H. Ultraclean Patterned Transfer of Single-Layer Graphene by Recyclable Pressure Sensitive Adhesive Films. *Nano Lett.* **2015**, *15*, 3236−3240.
(54) Hwang, E. H.; Das Sarma, S. Dielectric Function, Screening, and Plasmons in Two-Dimensional Graphene. *Phys. Rev. B: Condens. Matter Mater. Phys.* **2007**, *75*, 205418.
(55) Song, J. C. W.; Reizer, M. Y.; Levitov, L. S. Disorder-Assisted Electron-Phonon Scattering and Cooling Pathways in Graphene. *Phys. Rev. Lett.* **2012**, *109*, 106602.
(56) Graham, M. W.; Shi, S.-F.; Ralph, D. C.; Park, J.; McEuen, P. L. Photocurrent Measurements of Supercollision Cooling in Graphene. *Nat. Phys.* **2013**, *9*, 103−108.
(57) Betz, A. C.; Jhang, S. H.; Pallecchi, E.; Ferreira, R.; Fève, G.; Berroir, J.-M.; Plaçais, B. Supercollision Cooling in Undoped Graphene. *Nat. Phys.* **2013**, *9*, 109−112.
(58) Haus, H. A. *Waves and Fields in Optoelectronics*; Prentice Hall: Englewood Cliffs, NJ, 1984.
(59) Thongrattanasiri, S.; Koppens, F. H. L.; García de Abajo, F. J. Complete Optical Absorption in Periodically Patterned Graphene. *Phys. Rev. Lett.* **2012**, *108*, 047401.
(60) Woessner, A.; Lundeberg, M. B.; Gao, Y.; Principi, A.; Alonso-González, P.; Carrega, M.; Watanabe, K.; Taniguchi, T.; Vignale, G.; Polini, M.; Hone, J.; Hillenbrand, R.; Koppens, F. H. L. Highly Confined Low-Loss Plasmons in Graphene−Boron Nitride Heterostructures. *Nat. Mater.* **2015**, *14*, 421−425.
(61) Daniels, K. M.; Jadidi, M. M.; Sushkov, A. B.; Nath, A.; Boyd, A. K.; Sridhara, K.; Drew, H. D.; Murphy, T. E.; Myers-Ward, R. L.; Gaskill, D. K. Narrow Plasmon Resonances Enabled by Quasifreestanding Bilayer Epitaxial Graphene. *2D Mater.* **2017**, *4*, 025034.
(62) Wang, L.; Meric, I.; Huang, P. Y.; Gao, Q.; Gao, Y.; Tran, H.; Taniguchi, T.; Watanabe, K.; Campos, L. M.; Muller, D. A.; Guo, J.; Kim, P.; Hone, J.; Shepard, K. L.; Dean, C. R. One-Dimensional Electrical Contact to a Two-Dimensional Material. *Science* **2013**, *342*, 614−617.
(63) Brongersma, M. L.; Halas, N. J.; Nordlander, P. Plasmon Induced Hot Carrier Science and Technology. *Nat. Nanotechnol.* **2015**, *10*, 25−34.

DOI: 10.1021/acsphotonics.9b01037
ACS Photonics 2019, 6, 2562−2569